LETTER

Design of inertial fusion implosions reaching the burning plasma regime

A. L. Kritcher[1,*], C. V. Young[1,*], H. F. Robey[2,*], C. R. Weber[1], A. B. Zylstra[1], O. A. Hurricane[1], D. A. Callahan[1], J. E. Ralph[1], J. S. Ross[1], K. L. Baker[1], D. T. Casey[1], D. S. Clark[1], T. Döeppner[1], L. Divol[1], M. Hohenberger[1], S. Le Pape[3], A. E. Pak[1], P. K. Patel[1], R. Tommasini[1], S. J. Ali[1], P. A. Amendt[1], J. Atherton[1], B. Bachmann[1], D. Bailey[1], L. R. Benedetti[1], L. Berzak Hopkins[1], R. Betti[4], S. D. Bhandarkar[1], R. M. Bionta[1], N. W. Birge[2], E. J. Bond[1], D. K. Bradley[1], T. Braun[1], T. M. Briggs[1], M. W. Bruhn[1], P. M. Celliers[1], B. Chang[1], T. Chapman[1], H. Chen[1], C. Choate[1], A. R. Christopherson[1], J. W. Crippen[5], E. L. Dewald[1], T. R. Dittrich[1], M. J. Edwards[1], W. A. Farmer[1], J. E. Field[1], D. Fittinghoff[1], J. Frenje[6], J. Gaffney[1], M. Gatu Johnson[6], S. H. Glenzer[7], G. P. Grim[1], S. Haan[1], K. D. Hahn[1], G. N. Hall[1], B. A. Hammel[1], J. Harte[1], E. Hartouni[1], J. E. Heebner[1], V. J. Hernandez[1], H. Herrmann[2], M. C. Herrmann[1], D. E. Hinkel[1], D. D. Ho[1], J. P. Holder[1], W. W. Hsing[1], H. Huang[5], K. D. Humbird[1], N. Izumi[1], J. Jeet[1], O. Jones[1], G. D. Kerbel[1], S. M. Kerr[1], S. F. Khan[1], J. Kilkenny[5], Y. Kim[2], H. Geppert Kleinrath[2], V. Geppert Kleinrath[2], J. L. Kline[2], C. Kong[5], J. M. Koning[1], J. J. Kroll[1], O. L. Landen[1], S. Langer[1], D. Larson[1], N. C. Lemos[1], J. D. Lindl[1], T. Ma[1], B. J. MacGowan[1], A. J. Mackinnon[1], S. A. MacLaren[1], A. G. MacPhee[1], M. M. Marinak[1], D. A. Mariscal[1], E. V. Marley[1], L. Masse[1], K. Meaney[2], N. B. Meezan[1], P. A. Michel[1], M. A. Millot[1], J. L. Milovich[1], J. D. Moody[1], A. S. Moore[1], J. W. Morton[8], K. Newman[1], J.-M. G. Di Nicola[1], A. Nikroo[1], R. Nora[1], M. V. Patel[1], L. J. Pelz[1], J. L. Peterson[1], Y. Ping[1], B. B. Pollock[1], M. Ratledge[5], N. G. Rice[5], H. Rinderknecht[4], M. Rosen[1], M. S. Rubery[8], J. D. Salmonson[1], J. Sater[1], S. Schiaffino[1], D. J. Schlossberg[1], M. B. Schneider[1], C. R. Schroeder[1], H. A. Scott[1], S. M. Sepke[1], K. Sequoia[5], M. W. Sherlock[1], S. Shin[1], V. A. Smalyuk[1], B. K. Spears[1], P. T. Springer[1], M. Stadermann[1], S. Stoupin[1], D. J. Strozzi[1], L. J. Suter[1], C. A. Thomas[4], R. P. J. Town[1], E. R. Tubman[1], P. L. Volegov[2], K. Widmann[1], C. Wild[9], C. H. Wilde[2], B. M. Van Wonterghem[1], D. T. Woods[1], B. N. Woodworth[1], M. Yamaguchi[5], S. T. Yang[1], and G. B. Zimmerman[1]

[1] Lawrence Livermore National Laboratory, P.O. Box 808, Livermore, California 94551-0808, USA
[2] Los Alamos National Laboratory, Mail Stop F663, Los Alamos, New Mexico 87545, USA
[3] Laboratoire pour l'utilisation des Lasers Intenses chez École Polytechnique, F-91128 Palaiseau cedex, France
[4] Laboratory for Laser Energetics, University of Rochester, Rochester, New York 14623, USA
[5] General Atomics, San Diego, California 92186, USA
[6] Massachusetts Institute of Technology, Cambridge, Massachusetts 02139, USA
[7] SLAC National Accelerator Laboratory, Menlo Park, California 94025, USA
[8] Atomic Weapons Establishment, Aldermaston, RG7 4PR, United Kingdom
[9] Diamond Materials Gmbh, 79108 Freiburg, Germany
* These authors contributed equally: A. L. Kritcher, C. V. Young, H. F. Robey

One of the last remaining milestones in fusion research before reaching ignition is creating a burning plasma state,[1–6] where alpha particles from deuterium-tritium (DT) fusion reactions redeposit their energy as the dominant source of heating in the plasma. The indirect-drive inertial confinement fusion[7] approach at the National Ignition Facility (NIF)[8] uses a laser-generated radiation cavity (hohlraum) to spherically implode DT fuel to high temperatures and densities in a central "hot spot". Here, we deliver more energy to the hot spot than ever before, while maintaining the extreme pressures required for inertial confinement, by increasing the size of the implosion compared to previous experiments.[9,10] We develop more efficient hohlraums, to drive these larger implosions within NIF's current laser energy and power capability and control symmetry by moving energy between laser beams[11–16] and by changing the shape of the hohlraum.[17] These designs resulted in record fusion powers of 1.5 petawatts, greater than the input power of the laser, and 170 kJ of fusion energy.[18,19] Radiation hydrodynamics simulations show alpha particle heating as the dominant term in the hot spot energy balance, e.g. a burning plasma state. This work is expected to motivate future studies of burning plasmas and improve predictive capability by providing a benchmark for modeling used to understand the proximity to ignition.

Inertially confined fusion plasmas use a rocket-like ablation effect to compress millimeter size capsules filled with Deuterium-Tritium (DT) to hundreds of billions times the pressure of earth's atmosphere, the conditions required for a significant amount of fusion to occur. The rocket is created when the outer layers of the nuclear fuel-containing capsules are ablated by an intense x-ray radiation bath that is generated when the 192 laser beams of the National Ignition Facility laser illuminate the inside of a gold-lined depleted uranium x-ray conversion cavity called a "hohlraum." The remaining capsule mass and fuel is accelerated toward the center of the DT gas core at extreme implosion velocities (v_{imp}) of nearly 400 km/s. During stagnation, the kinetic energy of the imploding shell and DT fuel is converted to internal in a dense fuel layer surrounding a central lower density "hot spot" where most of the fusion reactions occur. Adequate symmetric compression of the DT fuel surrounding the hot spot is essential for providing inertial confinement of the hot spot for about 150 picoseconds, giving the implosion time to further heat itself from the alpha particles that are generated in the fusion reaction, leading to amplified fusion reactions and neutron yield.

The DT fuel is more compressible when the entropy is lower, e.g. lower fuel adiabat (α = plasma pressure / Fermi pressure), which is managed by raising the ablation pressure ($P_{\rm abl}$) in steps before accelerating the shell inwards, each step generating a limited amount of shock compression. After maximum ablation pressure is achieved, it is im-

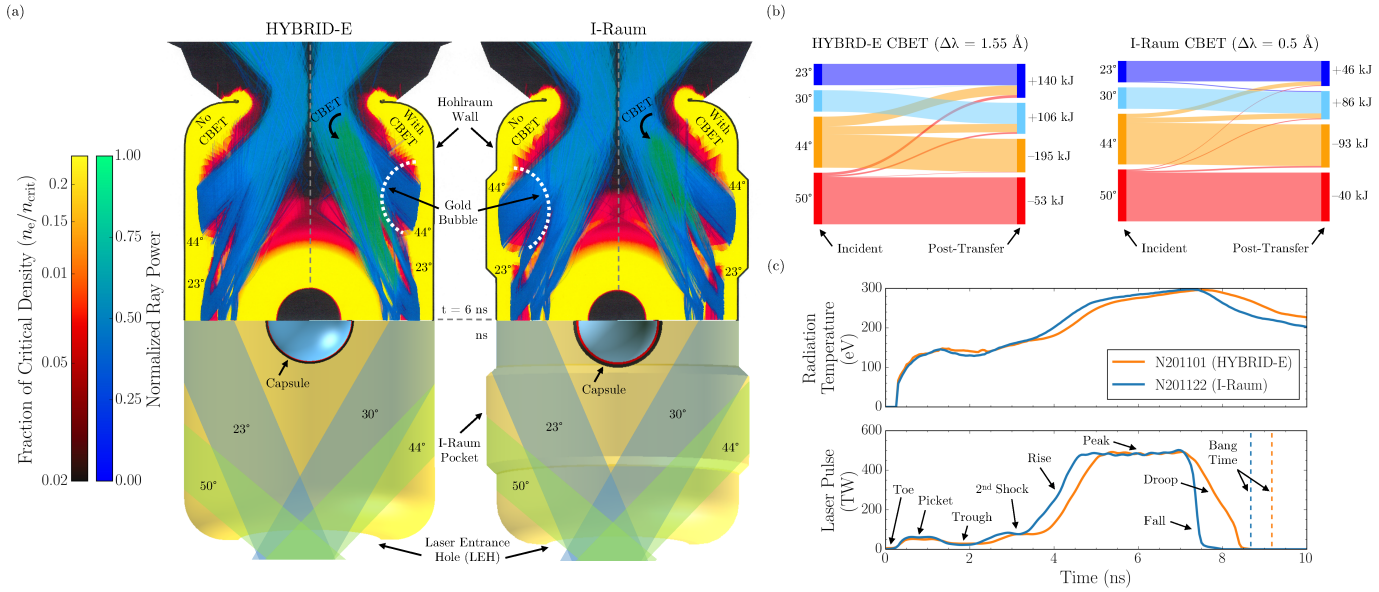

Fig. 1 | Hohlraum design for larger scale capsules. Implosion symmetry control in low gas fill hohlraums is accomplished via cross-beam energy transfer (CBET)[11,12,14–16] from the outer laser beams (44° and 50°) to the inners (23° and 30°) to compensate for reduced inner beam propagation later in time. The amount of transfer is controlled by detuning the wavelengths of the inner and outer cones relative to each other ($\Delta\lambda$). (a) The Hybrid-E cylindrical hohlraum (left) uses more CBET than the I-Raum shaped hohlraum (right) to achieve similar x-ray flux symmetry on the capsule since the I-Raum "pockets" radially displace the expanding wall plasma from the outers, delaying interception of the inners. The top of each hohlraum shows color maps of electron density, n_e, calculated at peak power (6 ns) from radiation-hydrodynamic HYDRA simulations with individual laser rays overlaid. Electron density is expressed as a fraction of the critical density, n_{crit}, at which the propagating laser frequency equals the local plasma frequency and inverse bremsstrahlung absorption occurs. Rays are colored by power, with some rays gaining power through CBET (more green) before becoming absorbed (more blue). The left sides depict simulations without wavelength detuning, while the right sides include $\Delta\lambda$, illustrating enhanced inner beam propagation due to CBET from a representative 44° to a 23° beam. The bottom half of each hohlraum depicts nominal beam pointing and relative target dimensions between the two designs as visualized by VISRAD.[20] (b) Energy flow diagrams illustrating the CBET process in more detail. The four cones of beams pass energy amongst themselves due to CBET from wavelength detuning ($\Delta\lambda$) and local plasma flows, resulting in a net gain for the inners and a net loss for the outers. (c) Measured hohlraum radiation temperatures using filtered x-ray diodes (top) and the delivered laser pulses (bottom) from two high performing shots from each design.

portant to maintain the ablation pressure as late into the implosion as possible to minimize fuel decompression prior to formation of the hot-spot. The number of neutrons produced from the fusion reactions, or neutron yield (Y), of an inertially confined fusion plasma mainly depends on a few key implosion properties together with the initial scale of the implosion (S), where larger implosions can result in a greater number of fusion reactions if the other properties can be maintained.[1]

$$Y = P_{\mathrm{abl}}^{16/25}\left(\frac{v_{\mathrm{imp}}^{67/15}}{\alpha^{36/25}}\right) S^{14/3}\,(1-\mathrm{RKE})^{23/7}\,\eta \qquad (1)$$

Measurable perturbations on the implosion can reduce the number of fusion reactions, such as non-sphericity in the imploding shell and fuel, as described by the residual kinetic energy (RKE),[23] ratio of unconverted fuel kinetic energy to hot spot compression and heating normalized to the total fuel kinetic energy. Shorter wavelength hydrodynamic instabilities lead to mixing of capsule material into the DT hot-spot which results in radiative loss or reduced compression and lower yield (η).[24] The degree to which hydrodynamic instabilities can impact the implosion depends on the stability of the target design, which itself depends upon the target geometry and laser pulse shape, as well as features in the target that can seed instabilities, e.g. defects in the capsule generated during fabrication, the fill tube used to fill the capsules with DT,[25] and the capsule support that holds the capsule in the center of the hohlraum.[26] The exponents in Eq. 1 were derived for an implosion where bremsstrahlung radiation losses balance alpha particle heating and are expected to change as the plasma starts to become dominated by alpha heating.

In this work we tripled the energy from fusion reactions compared to previous experiments by increasing the scale (S) of the implosion 10-15% and maintaining the other critical implosion properties in Eq. 1, a strategy outlined in Hurricane, *et.al.*,[1] to also maintain the hot spot pressure which is required for inertial confinement. Driving larger implosions to similar velocities as smaller scale implosions[9,10] using the same amount of laser energy, required developing more efficient hohlraums, smaller hohlraums compared to the size of the capsule (Case to Capsule Ratio (CCR)). Such designs are more challenging for symmetry as there is less room for the laser beams to propagate beyond the expanding capsule material and expanding wall plasma, resulting in radiation drive deficit deep in the interior of the hohlraum. The more intense "outer" laser beams (see Fig. 1 a) hit the wall closer to the ends of the hohlraum and create an expanding wall "bubble"[27,28] which intercepts the "inner" beams aimed at the center of the hohlraum. The resulting spatial non-uniformity in radiation temperature drives a non-spherical implosion that will reduce the implosion efficiency. Larger capsules also use thicker ablators to protect against the longer growth times for hydrodynamic instabilities, which requires longer duration laser pulses to preserve shock-timing, and more hohlraum plasma filling.

Implosion symmetry was previously controlled in small CCR hohlraums[29,30] by transferring energy between laser beams, but high

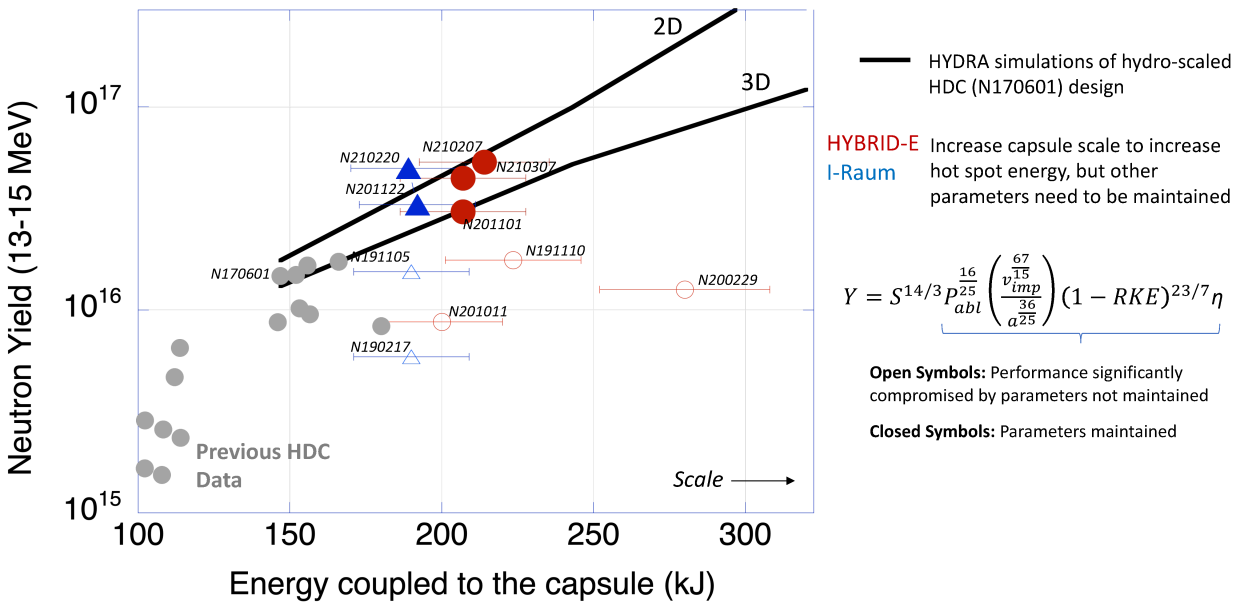

Fig. 2 | Proximity to expectations and optimization: Neutron yield as a function of capsule absorbed energy for the I-Raum (blue) and HYBRID-E (red) campaigns together with previous HDC experiments (grey points), and 2D and 3D simulations of scaling absorbed capsule energy from N170601[21] (solid black lines), showing agreement of this work with the more optimistic 2D predictions. Also shown are experiments in the I-Raum and HYBRID-E campaigns that led to the optimization in this work (open symbols) by also maintaining other important implosion properties in the yield equation (Eq. 1.), see the text.

levels of laser-plasma-interactions reduced the hohlraum efficiency by scattering laser light back out of the hohlraum. This was largely due to the application of large amounts of energy transfer in hohlraums with higher levels of Helium gas fill, designed to mitigate the expanding wall by generating a counter-pressure. These configurations also resulted in large amounts of inferred high energy electrons[31] that can prematurely heat the implosion. The entire time history of the radiation symmetry was also difficult to control and predict which resulted in non-spherical implosions and were a main source of performance degradation.[29,30,32] Since then, hohlraums with lower gas fill densities of 0.03- 0.6 mg/cm^3 with larger CCRs were developed[9,10,33–35] to reduce laser backscatter and hot electrons with no intentional energy transfer between laser beams, which used laser power balancing to control symmetry. This method of symmetry control limits the available laser energy and ultimately the implosion scale.

Here we introduce two designs that enabled increasing capsule scale within the limits of the NIF laser while providing symmetry control in more efficient smaller CCR hohlraums: transferring energy between laser beams by changing their relative wavelengths (wavelength detuning) in *lower* gas-filled hohlraums (HYBRID-E[11,13]) and using shaped hohlraums to delay plasma filling for better laser beam propagation (I-Raum[17]). The first technique transfers energy from the "outer" beams to the "inner" beams, increasing power delivered to the center of the hohlraum, in a low backscatter environment. Even in the presence of large amounts of transfer (up to 2X power increase on the inner beams) laser energy coupling to the hohlraum was $\geq$98%[11] and the level of inferred unwanted hot electrons was more than an order of magnitude lower than when using wavelength detuning in high gas-filled hohlraums. As a result of the reduced backscatter and laser plasma interactions, a stronger sensitivity of implosion symmetry to wavelength separation was observed and controlling the radiation symmetry through the entire drive history[11,23] in the presence of large amounts of transfer was possible. The HYBRID-E design is the first use of wavelength detuning in a hohlraum with gas fill density of 0.3 mg/cm^3 and for the first time in a diamond ablator design. The I-Raum[17] concept additionally uses engineered pockets in the wall to displace the outer-beam generated plasma radially outward, delaying expansion into the inner beams compared to a cylinder with the same pointing and pulse shape.

Figure 1 a) top shows radiation hydrodynamic simulations using HYDRA[36] of the two designs at 6.5 nanoseconds after the start of the laser picket together with the position of the expanding hohlraum wall "bubble"[27,28] (white dashed line), see the Methods for a description of the simulation methodology. The color contour is the ratio of electron density to the critical density (n_e/n_{crit}), the density at which the local plasma frequency matches the laser frequency and laser light becomes absorbed. Simulated laser rays show the impact of wavelength detuning on increasing the "inner" (23^o & 30^o) beam powers through CBET from the "outer" (44^o & 50^o) beams by comparing simulations with no detuning (left) to simulations that include the detuning (right), enhancing the drive at the waist of the hohlraum. Figure 1 b) also shows the total calculated energy transfer between the laser cones for the two designs. Less energy transfer between beams was required in the I-Raum design due to the pockets displacing the bubble outward, the smaller scale capsule, and the shorter laser pulse length as a result of a thinner DT ice layer (shorter shock transit time). The position of the bubble is similar for the two designs in this work as a result of other design difference that impact the bubble growth.[27,28] The measured radiation temperatures (T_r) (Fig. 1 c)) were similar given the the similar hohlraum surface areas. The laser power histories are also shown in Fig.1 c).

Figure 2 shows that the designs presented in this work realized the benefit of higher capsule absorbed energy (to increase energy delivered to the hot spot) compared to previous HDC implosions (grey points) by operating at larger scale, through improving or maintaining the other metrics in equation 1. Radiation hydrodynamic simulations[21] benchmarked against a smaller scale HDC implosion N170601 in two and three dimensions were extrapolated to higher levels of capsule absorbed

		N201101 (HYBRID-E)		N201122 (I-Raum)		N210207 (HYBRID-E)		N210220 (I-Raum)	
		Data	Simulation	Data	Simulation	Data	Simulation	Data	Simulation
Simulated Implosion Properties	Total Neutron Yield ($\times 10^{16}$)	3.49 ± 0.10	3.15	3.77 ± 0.12	3.75	6.07 ± 0.17	6.15	5.70 ± 0.15	5.34
	Fusion Energy, $E_{\rm fus}$ (kJ)	98.4 ± 2.7	89	106.1 ± 3.4	106	171.0 ± 4.8	173	160.6 ± 4.2	151
	Alpha Energy, $E_\alpha = E_{\rm fus}/5$ (kJ)	19.68 ± 0.54	17.8	21.22 ± 0.68	21	34.2 ± 0.96	34.6	32.12 ± 0.84	30.2
	γ Bang Time (ns)	9.37 ± 0.03	9.34	8.67 ± 0.03	8.67	9.09 ± 0.02	9.075	8.79 ± 0.03	8.79
	γ Burn Width (ps)	141 ± 30	97	150 ± 20	124	137 ± 30	107	139 ± 20	127
	X-ray Bang Time (ns)	9.37 ± 0.05	9.35	8.67 ± 0.03	8.67	9.13 ± 0.04	9.075	8.79 ± 0.03	8.80
	X-ray Burn Width (ps)	116 ± 6	110	133 ± 7	133	99 ± 6	114	134 ± 7	145
	DT Ion Temperature (keV)	4.95 ± 0.12	6.12	5.17 ± 0.13	5.50	5.66 ± 0.13	6.2	5.54 ± 0.14	5.64
	DD Ion Temperature (keV)	4.61 ± 0.14	5.35	4.65 ± 0.14	5.03	5.23 ± 0.16	5.4	5.13 ± 0.24	5.46
	DSR (4π, %)	3.44 ± 0.16	3.95	3.33 ± 0.14	3.42	3.16 ± 0.16	3.75	3.31 ± 0.14	3.54
	13–15 MeV Neutron P_0 (μm)	38.5 ± 1.1	39	38.9 ± 1.1	42.4	42.3 ± 1.1	41	37.6 ± 3.0	42.1
	13–15 MeV Neutron P_2 (μm)	8.0 ± 0.3	8	-5.1 ± 0.8	0.7	2.7 ± 0.2	5.33	-2.8 ± 0.4	-1.4
Simulated Energy Balance Quantities	1D Adiabat	–	3.0	–	3.2	–	3.0	–	3.1
	HS density (gm/cm^3)	–	76.9	–	62.9	–	75.1	–	66.3
	HS ρ (gm/cm^2)	–	0.32	–	0.3	–	0.32	–	0.33
	Implosion Velocity (km/s)	–	383	–	376	–	389	–	369
	DT Kinetic Energy (KE) (kJ)	–	15.45	–	11.68	–	15.83	–	11.18
	Deceleration Time (ns)	–	0.530	–		–	0.460	–	
	Radius at Peak Velocity (μm)	–	219	–		–	225	–	
	DT $E_{PdV,Fuel}$ (no-α) (kJ)*	–	21.1	–	16.91	–	19.72	–	17.03
	HS E_α (kJ) * ζ	–	9.73	–	12.6	–	20.08	–	17.8
	HS E_{rad} (kJ) * ζ	–	7.6	–	9.5	–	10.7	–	11.7
	HS E_{IE} (kJ) * ζ	–	14.42	–	15.7	–	19.04	–	18.6
	HS $E_{PdV,HS}$ (kJ) * ζ	–	13.4	–	12	–	13.1	–	12.6
	HS $E_{PdV,HS}$ (no-α) (kJ) * ζ	–	12.2	–	11.6	–	12.1	–	11.8
	HS E_α / E_{rad} * ζ	–	1.28	–	1.32	–	1.88	–	1.52
	HS E_α / E_{PdV} * ζ	–	0.73	–	1.05	–	1.53	–	1.41
	HS E_α / E_{IE} * ζ	–	0.67	–	0.8	–	1.05	–	0.96
B. P. Criteria	$E_\alpha^{*,\zeta}/E_{PdV,no-\alpha}$ * ζ (Betti^2) [>1]	–	0.8	–	1.09	–	1.66	–	1.51
	$0.5E_{\alpha,meas}/E_{PdV,no-\alpha}$ * ζ (Betti^2) [>1]	–	0.81	–	0.894	–	1.43	–	1.37
	$E_{\alpha,meas}/KE$ [>1]	–	1.28	–	1.77	–	2.17	–	2.88
	$Y_{\rm amp}$ [>3.5]	–	3.53	–	3.94	–	5.54	–	5.34
	$G_{\rm fuel} = E_{fusion}/\ E_{PdV,Fuel}$ [>5]	–	4.7	–	5.19	–	8.20	–	7.84
	$v_{\rm cond}/v_{\rm imp}$ (Hurricane[1]) [>1]	–	1.46	–	1.18	–	1.43	–	1.65

*Denotes quantity reported at "bang time," or time of peak neutron production and ζ denotes quantities extracted from Fig.3at bang time.

Table 1 | Integrated implosion metrics. Comparison of integrated implosion quantities between experiments and 2D radiation-hydrodynamic simulations with known degradation mechanisms included (see text). From these simulations we extract time histories of quantities comprising the hot spot power balance (see Fig. 3), and derive metrics like total PdV work done on the hotspot and yield amplification due to alpha heating. The fusion burn history is measured using both gamma (γ) particle and x-ray emission, where "bang time" denotes the time of peak neutron production. The neutron downscattered ratio (DSR) is the number of (downscattered) neutrons measured with energies 6–12 MeV divided by the number of primary neutrons with energies 13–15 MeV. The 4π DSR represents an average value over the full sphere, inferred by applying corrections to the values returned by the five neutron time-of-flight (NTOF) detectors positioned at different lines of sight around the NIF target chamber. Asymmetries in the x-ray and neutron emission images are reported as coefficients of a Legendre mode decomposition, where P_n represents the coefficient of the $n^{\rm th}$ mode. Deceleration time is defined as the difference between the times of peak neutron production and maximum implosion velocity. Yield amplification is defined as the ratio of total yields produced in a pair of simulations in which alpha particles either deposit energy in the hotspot ("burn on") or stream freely out of the problem ("burn off", no-α).

energy while maintaining the symmetry, stability, implosion velocity, adiabat, and inflight ablation pressure. The results of this work, I-Raum (blue) and HYBRID-E (red), follow the more optimistic extrapolation in two dimensions which suffers less from perturbations that can lower the yield. The larger scale I-Raum and HYBRID-E designs absorb more energy but also use larger hohlraums (lower Tr) to maintain symmetry and require thicker ablators or DT layers to maintain stability (see the methods for a description of these designs compared to a hydroscale design of N170601) which results in similar implosion velocities, see Table 1. At similar radiation temperatures, HYBRID-E absorbs more energy than I-Raum due to the larger capsule scale but also drives a thicker DT fuel layer and ramping down the end of the laser pulse to maintain ablation pressure at larger scale, see the Methods. Due to the shock mergers being $\sim$10μm deep in the DT ice, the fuel adiabats at peak velocity were a little higher for both designs ($3-3.2$) compared to N170601 (2.5), see Table 1, suggesting room for additional improvement in performance.

The progression of the design or experimental optimization within the HYBRID-E and I-Raum campaigns is shown through several example points (open symbols) which illustrates that the benefit of increased capsule energy can only be realized if the pressure is maintained through the other terms in Equation 1. Both designs have worked to maintain the late time ablation pressure but continued optimization is ongoing. A metric for this is the the "coast time",[22] or time that the implosion has to decompress when the radiation drive is decreasing (Table 1 and the methods), which was reduced between experiments N201011 and N201110 by extending the laser pulse and resulted in >3 times the neutron yield. Experiment N200229 had more coupled energy to the capsule than the experiments in this paper using a larger capsule scale (1100μm inner radius) but the "coast time" was $\sim 1.7X$ longer, the symmetry was significantly worse, and the number of seeds for high mode perturbations in the ablator were significantly worse,[19] reducing the implosion efficiency η. I-Raum experiments N190217 vs N191105 also showed the impact of improving high mode instabilities on the neutron yield by reducing the number of ablator defects and improving the design stability using a higher picket. Capsule defects that

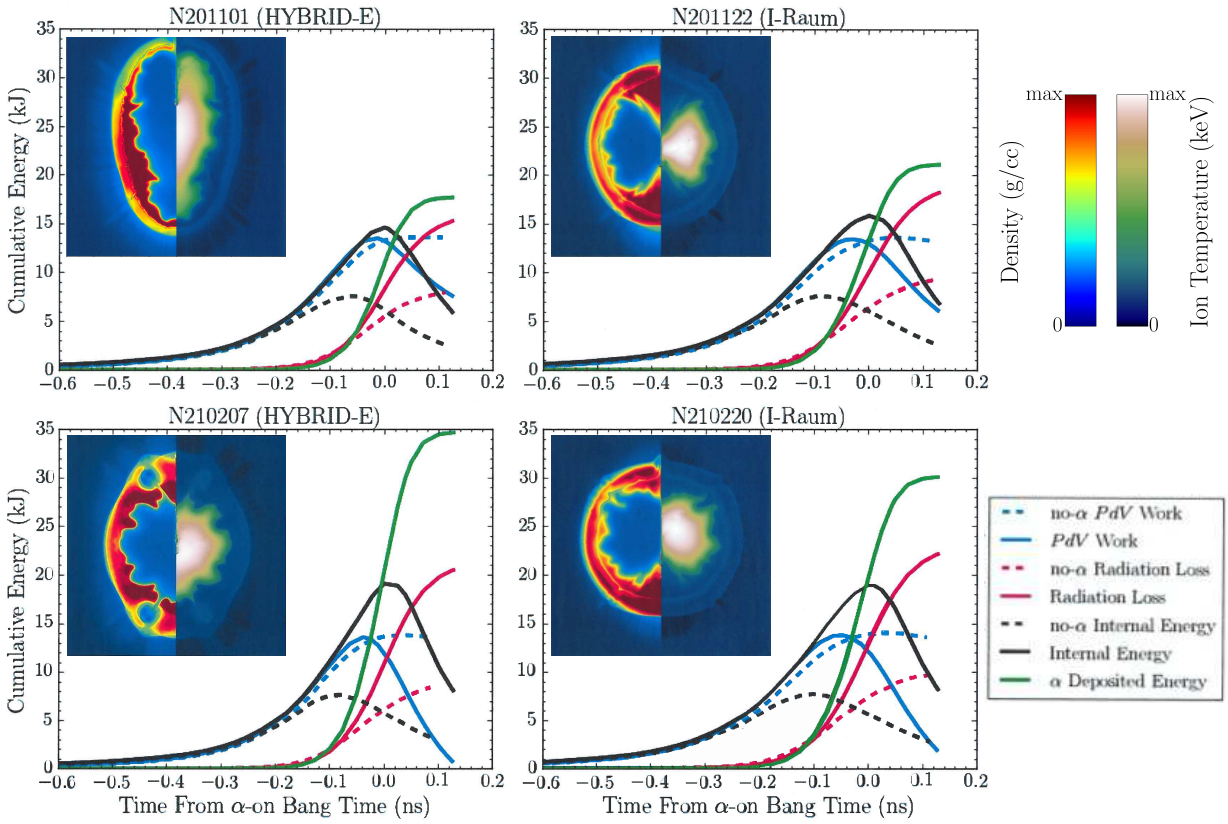

Fig. 3 | Hotspot energy partition in the burning plasma regime. Calculated cumulative hotspot energies as a function of time (see Eqn. **??**) for each shot. Each panel shows data from one "burn on" simulation that includes alpha deposition (α-on, solid curves) and one "burn off" simulation in which alpha particles leave the problem without depositing energy (α-off, dashed curves). The time axis has been scaled relative to the "bang time," or time of peak neutron production, for each simulation with alpha deposition included. The respective (α-on, α-off) bang times in nanoseconds for shots N201101, N201122, N210207, and N210220 are: (9.35, 9.30), (9.08, 9.03), (8.67, 8.60), (8.80, 8.70). The total hotspot internal energy (black) is increased due to hydrodynamic compression (PdV work, blue) up until stagnation and any alpha heating (green), and is reduced due to Bremsstrahlung radiation losses (red) and hydrodynamic expansion after stagnation (PdV work, blue). For these experiments entering the burning plasma regime, the alpha particle heating outstrips the radiation losses, becoming the dominant term in the hotspot energy balance. The inset images illustrate the simulated configuration of the hotspot and dense surrounding shell with density (g/cc) on the left half and ion temperature (keV) on the right half. The hotspot is defined as a fixed collection of DT mass, tracked over time, that gives 98% of the neutron production at peak burn. The respective maximum (density, ion temperature) values for shots N201101, N201122, N210207, and N210220 in (g/cc, keV) are: (350, 7.31), (450, 6.49), (350, 8.4), (450, 7.2).

can seed high mode perturbations, other than the support tent and DT fill tube, are still present in the HYBRID-E experiments[19] and further improvement could lead to higher performance.[19] Both designs are predicted to have increased performance with reduction of the DT fill tube size which can result in ablator mix into the hot spot,[19] experiments to test this are ongoing.

Improving the low mode radiation drive asymmetries, which is challenging at larger scale, also led to realization of the benefit of increased absorbed energy. This is shown by the >2X increase in performance of I-Raum designs N201122 and N210220 compared to N191105 which improved symmetry by introducing a small amount of wavelength detuning ($\Delta\lambda$=0.5 $\AA$). HYBRID-E experiments also improved symmetry by dialing down the amount of wavelength detuning between experiments N201101 (1.75 Angstroms) vs N210307 and N210207 (1.55 Angstroms), improving performance by 40-70%. Both designs control the time-dependent radiation flux symmetry during the early part of the laser pulse using fine tuning of the laser power balance, see the methods. While the intrinsic low mode asymmetries were improved to reach high performance, as-shot laser power variations and target non-uniformities resulted in odd mode asymmetries that are calculated to impact the performance, and are worse for the I-Raum experiments.[19] Additional tests to reduce these non-uniformities are ongoing. Finally, while the results of this work agree with the more optimistic projections,[21] the calculated compression is higher than measured as diagnosed through the ratio of neurons down-scattered by the dense fuel (DSR), see Table 1. Designs to improve the compression and hot spot pressure by enhancing the linear stability at higher capsule absorbed energy are ongoing.

By increasing the hot spot energy with more coupled energy to the implosion, while also maintaining the hot spot pressure, we have created a burning plasma state in the laboratory for the first time. The criteria for achieving a burning plasma state are investigated using analytical models[18] and key quantities derived from high resolution two dimensional HYDRA simulations that reproduce performance metrics, see the methods and Table 1. The mechanical PdV work (E_{PdV}) on the hot spot and total DT fuel from the imploding DT ice and ablator material are directly extracted from the simulations, see the methods. Net cumulative hot spot energies as a function of time relative to the time of peak neutron production ("bang-time") are shown in Fig.3 together with insets of the simulated densities and temperatures at bang-

time. Simulations where alpha particle heating is artificially turned off ($no-\alpha$) are also shown and enable more accurate tracking of the mechanical work.

We find that the net energy from alpha particle heating at bang time ($E_\alpha^{*,\zeta}$) is greater than the work done on the hot spot (E_{PdV}) for three of the four experiments, and is thus the dominant source in the energy balance equation ($E_{\rm IE} = E_\alpha + E_{PdV} - E_{\rm rad} - E_{\rm cond}$). While the simulated metric for all four experiments is met ($E_\alpha^{*,\zeta}/E_{PdV,no-\alpha}$ >1), the more simplistic metric of $\sim 0.5E_\alpha/E_{PdV,HS,no-\alpha}$ >1 is only met by the two highest performing experiments. The net energy from alpha particle heating is calculated to be greater than the energy loss terms from radiation and conduction for all experiments ($E_{\rm rad}$, $E_{\rm cond}$) and greater than the hot spot internal energy (E_{IE}) for one experiment N210207. Here, the radiation losses are extracted from the simulations and conduction losses are inferred from the energy balance equation.

Other metrics for a burning plasma include the ratio of total the total energy produced by the alpha particles to the total DT kinetic energy (E_α/KE >1) which is met by all four experiments. Additionally, the yield amplification, increase in yield due to alpha particle heating ($Y_{amp} \geq 3.5$[2]) is met by all four experiments and the fuel gain (G_{fuel}[29]), ratio of the total fusion yield to the total PdV work done on the hot spot and compressed DT ice (DT $E_{PdV,no-\alpha}$) is met by three experiments and close for N201101. Finally, the Hurricane model for assessing a burning plasma state using the simulated hot spot areal density, ion temperature, and implosion velocity (v_{cond}/v_{imp}) is met by all four experiments. In summary, N210207 meets all criteria and also dominates the energy balance equation including hot spot internal energy, two experiments meet all of the criteria, and all four experiments meet several of the criteria for a burning plasma.

In summary, we have created a burning plasma state in the laboratory for the first time with two different design platforms and are using the results to benchmark simulation models that are used to assess proximity to ignition. These computational models were required to generate and optimize the designs, together with analytical scalings, and are used to assess the burning-plasma criteria including the hot spot energy balance. A burning plasma state was achieved by increasing the hot spot energy, through improving hohlraum efficiency, and capsule absorbed energy at fixed laser energy, while maintaining other important implosion properties. Future experiments will continue to optimize these platforms by reducing the sources of high mode perturbations (e.g. capsule defects and the DT fill tube), reduce the adiabat by improving shock timing and the rate of the final rise to peak laser power, and improve hot spot pressure or energy coupling with even more efficient hohlraums or by varying the DT ice thickness, see the Methods. These improvements are calculated to have large impacts in performance, e.g. reducing the "coast-time" with a smaller LEH is calculated to improve performance by $\sim 2X$ for both platforms. In addition, we continue to study the tradeoffs between ablator and DT thickness ratios for large scale implosions, which is important for understating limitations on design choices for future designs that additionally increased scale beyond the designs in this paper.

Data Availability

Experimental data used for this manuscript are available upon reasonable request. The simulation codes used in this manuscript are not available to the general public.

References

1. O A Hurricane, D A Callahan, P T Springer, M J Edwards, P Patel, K Baker, D T Casey, L Divol, T Döeppner, D E Hinkel, L F Berzak Hopkins, A Kritcher, S Le Pape, S Maclaren, L Masse, A Pak1, L Pickworth, J Ralph, C Thomas, A Yi and A Zylstra, *Plasma Physics and Controlled Fusion* **61**, 014033 (2019).
2. R. Betti, A. R. Christopherson, B. K. Spears, R. Nora, A. Bose, J. Howard, K. M. Woo, M. J. Edwards, and J. Sanz, *Phys. Rev. Lett.* **114**, 255003 (2015).
3. O. A. Hurricane, P. T. Springer, P. K. Patel, D. A. Callahan, K. Baker, D. T. Casey, L. Divol, T. Döeppner, D. E. Hinkel, M. Hohenberger, L. F. Berzak Hopkins, C. Jarrott, A. Kritcher, S. Le Pape, S. Maclaren, L. Masse, A. Pak, J. Ralph, C. Thomas, P. Volegov, and A. Zylstra, *Physics of Plasmas* **26**, 052704 (2019).
4. Mauel, M. et al., *Final Report of the Committee on a Strategic Plan for U.S. Burning Plasma Research,National Academies Press,Washington, D.C.* , (2019).
5. J. D. Lindl, S. W. Haan, O. L. Landen, A. R. Christopherson, and R. Betti, *Physics of Plasmas* **25**, 122704 (2018).
6. A. R. Christopherson, R. Betti, S. Miller, V. Gopalaswamy, O. M. Mannion, and D. Cao, *Physics of Plasmas* **27**, 052708 (2020).
7. Atzeni, S. & Meyer-ter-Vehn J., *The Physics of Inertial Fusion. Beam Plasma Interaction, Hydrodynamics, Hot Dense Matter* , Oxford Univ. Press (2004).
8. Edward Moses, *Astrophysics and Space Science* **336**, 3-7(2011).
9. S. Le Pape, L.?F. Berzak Hopkins, L. Divol, A. Pak, E.?L. Dewald, S. Bhandarkar, L.R. Bennedetti, T. Bunn, J. Biener, J. Crippen, D. Casey, D. Edgell, *Phys. Rev. Lett.* **120**, 245003(2018).
10. D. T. Casey, C. A. Thomas, K. L. Baker, B. K. Spears, M. Hohenberger, S. F. Khan, R. C. Nora, C. R. Weber, D. T. Woods, O. A. Hurricane, D. A. Callahan, R. L. Berger, J. L. Milovich, P. K. Patel, T. Ma, A. Pak, L. R. Benedetti, M. Millot, C. Jarrott, et al., *Physics of Plasmas* **25**, 056308(2018).
11. A. L. Kritcher, A. B. Zylstra, D. A. Callahan, O. A. Hurricane, C. Weber, J. Ralph, D. T. Casey, A. Pak, K. Baker, B. Bachmann, S. Bhandarkar, J. Biener, et al., *Physics of Plasmas* , (2021).
12. A. L. Kritcher, J. Ralph, D. E. Hinkel, T. Döeppner, M. Millot, D. Mariscal, R. Benedetti, D. J. Strozzi, T. Chapman, C. Goyon, B. MacGowan, P. Michel, D. A. Callahan, and O. A. Hurricane, *Phys. Rev. E* **98**, 053206 (2018).
13. A.B. Zylstra, A.L. Kritcher, O.A. Hurricane, D.A. Callahan, K. Baker, T. Braun, D.T. Casey, D. Clark, K. Clark, T. Döeppner, et al, *Phys. Rev. Lett.* **126**, 025001(2021).
14. W. L. Kruer, S. C. Wilks, B. B. Afeyan, and R. K. Kirkwood, Phys. Plasmas, *Phys. Plasmas* **3**, 382(1996).
15. S. H. Glenzer, B. J. MacGowan, P. Michel, N. B. Meezan, L. J. Suter, S. N. Dixit, J. L. Kline, G. A. Kyrala, D. K. Bradley, D. A. Callahan, E. L. Dewald, et al., *Science* **327**, 5970(2010).
16. P. Michel, L. Divol, E. A. Williams, S. Weber, C. A. Thomas, D. A. Callahan, S. W. Haan, J. D. Salmonson, S. Dixit, D. E. Hinkel, M. J. Edwards, et al., *Phys. Rev. Lett.* **102**, 025004(2009).
17. H. F. Robey, L. Berzak Hopkins, J. L. Milovich, and N. B. Meezan, *Physics of Plasmas* **25**, 012711(2018).
18. A.B. Zylstra, O.A. Hurricane, D.A. Callahan, A.L. Kritcher, J. Ralph, H.F. Robey, J.S. Ross, C. Young, K. Baker, D. Casey, T. Döeppner, et al, *Nature* , (2021).
19. J. S. Ross, J. E. Ralph, A. B. Zylstra, H. Robey, C. Young, A. L. Kritcher, O. A. Hurricane, B. Bachmann, R. Bionta, M. Bruhn, D. A. Callahan, et al,, *Nature Physics* , (2021).
20. J. MacFarlane, *Journal of Quantitative Spectroscopy and Radiative Transfer* **81**, 287-300(2003).
21. D. S. Clark, C. R. Weber, J. L. Milovich, A. E. Pak, D. T. Casey, B. A. Hammel, D. D. Ho, O. S. Jones, J. M. Koning, A. L. Kritcher et al., *Physics of Plasmas* **26**, 050601 (2019).
22. O. A. Hurricane, A. Kritcher, D. A. Callahan, O. Landen, P. K. Patel, P. T. Springer, D. T. Casey, E. L. Dewald, T. R. Dittrich, T. Döeppner et al., *Physics of Plasmas* **24**, 092706 (2017).
23. A. L. Kritcher, R. Town, D. Bradley, D. Clark, S. Spears, O. Jones, S. Haan, P. T. Springer, J. Lindl, R. H. H. Scott, D. Callahan, M. J. Edwards, O. L. Landen, *Phys of Plasmas* **21**, 042708(2014).
24. A. Pak, L. Divol, C.R. Weber, L.F. Berzak Hopkins, D.S. Clark, E.L. Dewald, D.N. Fittinghoff, V. Geppert-Kleinrath, M. Hohenberger, S. Le Pape, et al, *Phys. Rev. Lett.* **124**, 145001(2020).
25. K. L. Baker, C. A. Thomas, T. R. Dittrich, O. Landen, G. Kyrala, D. T. Casey, C. R. Weber, J. Milovich, D. T. Woods, M. Schneider, S. F. Khan, *Phys of Plasmas* **27**, 112706(2020).
26. S. R. Nagel, S. W. Haan, J. R. Rygg, M. Barrios, L. R. Benedetti, D. K. Bradley, J. E. Field, B. A. Hammel, N. Izumi, O. S. Jones, S. F. Khan, et al, *Phys of Plasmas* **22**, 022704(2015).
27. D. A. Callahan, O. A. Hurricane, J. E. Ralph, C. A. Thomas, K. L. Baker, L. R. Benedetti, L. F. Berzak Hopkins, D. T. Casey, T. Chapman, C. E. Czajka, E. L. Dewald, et al, *Phys of Plasmas* **25**, 056305(2018).
28. J. E. Ralph, O. Landen, L. Divol, A. Pak, T. Ma, D. A. Callahan, A. L. Kritcher, T. Doeppner, D. E. Hinkel, C. Jarrott, J. D. Moody, B. B. Pollock, O. Hurricane, and M. J. Edwards, *Phys of Plasmas* **25**, 082701(2018).

29. J. D. Lindl, O. L. Landen, J. Edwards, E. I. Moses, J. Adams, P. A. Amendt, N. Antipa, P. A. Arnold, L. J. Atherton, S. Azevedo, D. Barker, M. A. Barrios, et al.,, *Physics of Plasmas* **21**, 020501(2014).
30. O. A. Hurricane, D. A. Callahan, D. T. Casey, P. M. Celliers, C. Cerjan, E. L. Dewald, T. R. Dittrich, T. Döeppner, D. E. Hinkel, L. F. Berzak Hopkins, J. L. Kline, et al, *Nature* **506**, 343-348(2014).
31. E L Dewald, C Thomas, S Hunter, L Divol, N Meezan, S H Glenzer, L J Suter, E Bond, J L Kline, J Celeste, D Bradley, P Bell, R L Kauffman, J Kilkenny, O L Landen, *Rev Sci Instrum.* **81**, 10D938(2010).
32. A. L. Kritcher, D. E. Hinkel, D. A. Callahan, O. A. Hurricane, D. Clark, D. T. Casey, E. L. Dewald, T. R. Dittrich, T. Döeppner, M. A. Barrios Garcia, S. Haan, et al., *Phys. Plasmas* **23**, 052709(2016).
33. L. F. Berzak Hopkins, N. B. Meezan, S. Le Pape, L. Divol, A. J. Mackinnon, D. D. Ho, M. Hohenberger, O. S. Jones, G. Kyrala, J. L. Milovich, A. Pak, J. E. Ralph, et al, *Phys. Rev. Lett.* **114**, 175001(2015).
34. D. Turnbull, L. F. Berzak Hopkins, S. Le Pape, L. Divol, N. Meezan, O. L. Landen, D. D. Ho, A. Mackinnon, A. B. Zylstra, H. G. Rinderknecht, H. Sio, *et al.*, *Phys. Plasmas* **23**, 052710(2016).
35. L. Divol, A. Pak, L. F. Berzak Hopkins, S. Le Pape, N. B. Meezan, E. L. Dewald, D. D.-M. Ho, S. F. Khan, A. J. Mackinnon, J. S. Ross, D. P. Turnbull, C. Weber, *et al.*, *Phys. Plasmas* **24**, 056309(2017).
36. M. M. Marinak, G. D. Kerbel, N. A. Gentile, O. Jones, D. Munro, S. Pollaine, T. R. Dittrich, and S. W. Haan, *Phys. of Plasmas* **8**, 2275(2001).

Acknowledgements

This work was performed under the auspices of the U. S. Department of Energy by Lawrence Livermore National Laboratory under Contract DE-AC52-07NA27344. This document was prepared as an account of work sponsored by an agency of the United States government. Neither the United States government nor Lawrence Livermore National Security, LLC, nor any of their employees makes any warranty, expressed or implied, or assumes any legal liability or responsibility for the accuracy, completeness, or usefulness of any information, apparatus, product, or process disclosed, or represents that its use would not infringe privately owned rights. Reference herein to any specific commercial product, process, or service by trade name, trademark, manufacturer, or otherwise does not necessarily constitute or imply its endorsement, recommendation, or favoring by the United States government or Lawrence Livermore National Security, LLC. The views and opinions of authors expressed herein do not necessarily state or reflect those of the United States government or Lawrence Livermore National Security, LLC, and shall not be used for advertising or product endorsement purposes. LLNL-JRNL-XXXXXX-DRAFT

Author contributions

A.L.K. Hybrid-E design lead, integrated hohlraum group lead, wrote sections of paper; C.V.Y. present I-Raum design lead, wrote sections of paper; H.F.R. original I-Raum design lead; C.R.W. capsule/instability physics; A.B.Z. hot-spot analysis lead, Hybrid-E experimental lead; O.A.H. capsule scale/burning plasma strategy, theory, 0D hot-spot models, and wrote sections of paper; D.A.C. empirical hohlraum P_2 model and hohlraum strategy; J.E.R. N201101 & N210207 experimentalist and "Shot RI" (shot responsible individual); J.S.R. I-Raum experimental lead and N201122 Shot RI; K.L.B. Hybrid Shot RI; D.T.C. Hybrid Shot RI; T.D. Hybrid Shot RI; L.D. 3D hot-spot analysis; M.H. Hybrid Shot RI; S.L.P. Hybrid Shot RI; A.E.P. Hybrid & I-Raum Shot RI, physics of capsule engineering defects; P.K.P. 1D hot-spot analysis, Y_{amp} and GLC inference; R.T. Hybrid Shot RI; S.J.A. capsule microstructure physics; P.A.A. hohlraum physics; B.B. penumbral x-ray diagnostic; D.B. computational physics; L.R.B. x-ray framing camera; L.B.H. HDC design and campaign lead; R.B. ICF physics/ignition theory; S.D.B. cryo layering; R.M.B. RTNAD nuclear diagnostic; N.W.B. neutron diagnostics; E.J.B. project engineering; D.K.B. diagnostics; T.B. capsule fab & metrology; T.M.B. cryo layering; M.W.B. project engineering; P.M.C. DT EOS measurements; B.C. HYDRA code development; T.C. LPI physics; H.C. GLEH x-ray diagnostic; C.C. target fab planning; A.R.C. ignition theory; D.S.C. capsule/instability physics; J.W.C. capsule fabrication; E.L.D. experiments; T.R.D. capsule physics; M.J.E. program management; W.A.F. hohlraum physics; J.E.F. 2DConA image analysis; D.F. nuclear diagnostics; J.F. magnetic recoil spectrometer nuclear diagnostic; J.G. ensemble simulations; M.G.J. magnetic recoil spectrometer diagnostic; S.H.G. ICF physics; G.P.G. nuclear diagnostics; S.H. capsule physics, iPOM analysis; K.D.H. neutron diagnostics; G.N.H. experiments; B.A.H. capsule physics; J.H. computational physics; E.H. nuclear time-of-flight diagnostics; J.E.H. MOR and PAM stability, SSD improvements, and FC control; V.J.H. MOR and PAM stability, SSD improvements, and FC control; H.H. gamma diagnostics; M.C.H. program management; D.E.H. hohlraum physics, CBET studies in Hybrid-C; D.D.H. capsule physics; J.P.H. x-ray diagnostics; W.W.H. management; H.H. capsule fabrication; K.D.H. ensemble simulations; N.I. x-ray diagnostics; J.J. neutron diagnostics; O.J. hohlraum physics; G.D.K. HYDRA code development; S.M.K. neutron diagnostics; S.F.K. x-ray diagnostics and analysis; J.K. diagnostic management; Y.K. gamma diagnostics; H.G.K. gamma diagnostics; V.G.K. neutron diagnostics; J.L.K. hohlraum physics/diagnostic planning; C.K. capsules; J.M.K. HYDRA code development; J.J.K. targets; O.L.L. velocity analysis; S.L. laser plasma instability (PF3D) code development; D.L. NIF facility management; N.C.L. optical diagnostics; J.D.L. ICF physics; T.M. ICF physics; B.J.M. mode-1 analysis, backscatter; A.J.M. diagnostic management; S.A.M. integrated design physics; A.G.M. x-ray diagnostics; M.M.M. HYDRA code development lead; D.A.M. x-ray diagnostics; E.V.M. x-ray diagnostics; L.M. capsule physics; K.M. gamma diagnostics; N.B.M. hohlraum physics; P.A.M. LPI physics; M.A.M. optical diagnostics; J.L.M. hohlraum physics; J.D.M. hohlraum physics; A.S.M. neutron diagnostics; K.N. project engineering; J.G.D.N. MOR and PAM stability, SSD improvements, and FC control; A.N. target fab engineering, capsule, and fab planning; R.N. ensembles simulations; M.V.P. HYDRA code development; L.J.P. MOR and PAM stability, SSD improvements, and FC control; J.L.P. ensembles simulations; Y.P. hohlraum physics; B.B.P. hohlraum physics; M.R. capsule fabrication; N.G.R. capsule fabrication; H.R. RTNAD mode-1 analysis; M.R. hohlraum physics; M.S.R. x-ray diagnostics; J.D.S. hohlraum physics; J.S. mode-1 analysis; S.S. capsules; D.J.S. neutron diagnostics; M.B.S. hohlraum diagnostics; C.R.S. HYDRA code development; H.A.S. NLTE opacities (Cretin) code development; S.M.S. HYDRA code development; K.S. mode-1 metrology; M.W.S. kinetic physics; S.S. sagometer data & particle analysis; V.A.S. capsule physics; B.K.S. ensemble simulations; P.T.S. dynamic model, ignition theory; M.S. capsules; S.S. x-ray diagnostics; D.J.S. hohlraum/LPI physics; L.J.S. hohlraum physics; C.A.T. Bigfoot design physics; R.P.J.T. program management; E.R.T. optical diagnostics; P.L.V. neutron imaging diagnostics; K.W. x-ray diagnostics; C.W. capsule fabrication; C.H.W. neutron diagnostics; B.M.V.W. NIF operations lead; D.T.W. hohlraum physics; B.N.W. project engineering; M.Y. capsule fabrication; S.T.Y. MOR and PAM stability, SSD improvements, and FC control; G.B.Z. computational physics lead.

Competing interests

The authors declare no competing interests.

Additional information

Correspondence and requests for materials should be addressed to A. L. K. (kritcher2@llnl.gov) or C. V. Y. (young110@llnl.gov).

	N170601[9] (HDC)	N180128[10] (Bigfoot)	N201101 (HYBRID-E)	N201122 (I-Raum)	N210207 (HYBRID-E)	N210220 (I-Raum)
$\Delta\lambda$ (Angstroms)	0	0	1.75	0.5	1.55	0.5
DT ice thickness (μm)	55	49	65	55	65 [63.4]	55 [60.4]
Ablator inner radius (μm)	910	950	1050	1000	1050	1000
W Dopant layer %	0.33	0.28	0.44	0.42	0.28	0.42
Dopant thickness (μm)	20.2	21.4	18.5 (17.7)	23 (22)	20	23 (22)
Dopant optical depth	6.66	6.0	8.14 (7.8)	9.7 (9.2)	5.6 [5.7]	9.7 (9.2) [6]
Diamond Crystallinity	Micro	Micro	Nano	Nano	Micro	Nano
HDC density (g/cc)	3.48	3.48	3.32	3.32	3.48	3.32
Total shell thickness (μm)	70	72	79 (75.4)	83 (79)	76 [76.8]	83 (79) [74.3]

Table 2 | Additional Design Parameters: Inner and outer wavelength separation ($\Delta\lambda$) and additional ablator design dimensions and properties for the experiments in this work. The values in parentheses are the Micro-crystalline (MCD) equivalent thicknesses and optical depths, where optical depth is W dopant percent times dopant layer thickness (%xμm). The numbers in red brackets show the hydro-scaled [per Clark *et al*[21]] MCD equivalent optical depths, total ablator thicknesses, and DT ice thicknesses for the two highest performing HYBRID-E and I-Raum experiments compared to HDC (N170601).[9]

Methods

Additional Design Parameters

The HYBRID-E and I-Raum designs use similar hohlraum surface areas and length, and the same size of laser entrance holes (LEH), a main source of radiation loss, which led to similar radiation temperatures, see Fig.1. The HYBRID-E shots N201101 and N210207 use 1.75 and 1.55 Angstroms of wavelength separation, respectively, between the outer and inner beams to implode a 1050µm inner radius high density carbon (HDC) capsule filled with a 65µm thick frozen D-T "ice" layer (density ~0.25 g/cm^3) with sufficient drive at the hohlraum equator. The I-Raum shots N201122 and N210220 use 260µm recessed pockets together with 0.5 Angstroms of wavelength separation to drive a 1000µm inner radius diamond capsule filled with a 55µm thick frozen D-T "ice" layer. See Fig.4 for additional hohlraum design dimensions.

Both designs used an HDC abaltor (capsule) with either nanocrystalline or microcrystalline structure[1] and a tungsten dopant layer to act as a preheat shield from high energy hohlraum x-rays and provide a more stable Atwood number.[2,21] Both designs increase the ablator thickness compared to smaller scale implosions[9,10] which is required when hydro-scaling (hydrodynamic scaling) a design to shield against the longer time for hydrodynamic instabilities to grow. The I-Raum design used an ablator which was thicker (~14% in effective thickness) than the increase in capsule scale (~10% increase in capsule radius) compared to HDC.[9] The "effective" thickness accounts for the difference in crystalline structure between the designs (Microcrystalline for HDC and Bigfoot), which changes the HDC density. Nanocrystalline ablators have lower density and require thicker layers for the same "effective" layer thickness compared to Microcrystalline HDC. The HYBRID-E design increased the ablator thickness compared to the HDC design but was thinner than the increase in capsule scale (~10% thicker vs an increase in capsule scale of ~15%) although consistent with the prescription for hydro-scalling.[21] This choice was initially made, given the current radiation drive, to enable driving a thicker DT ice layer than hydro-scaled (~18% increase in thickness compared to a ~15% in capsule scale), to similar velocity, for the purpose of providing more protection against high mode perturbations from known capsule defects present in these specific capsule batches, and has previously been shown to be effective.[13] However, as found by Clark, *et al*,[21] the scaled ablator thickness should be thinned by 5μm for every 20% increase in scale, which is consistent with the HYBRID-E design thickness as a hydroscale of HDC[9] and Bigfoot.[10] The I-Raum design uses the same ice thickness as the HDC design, thinner than hydrodynamically scaled with the capsule radius, which may enable higher

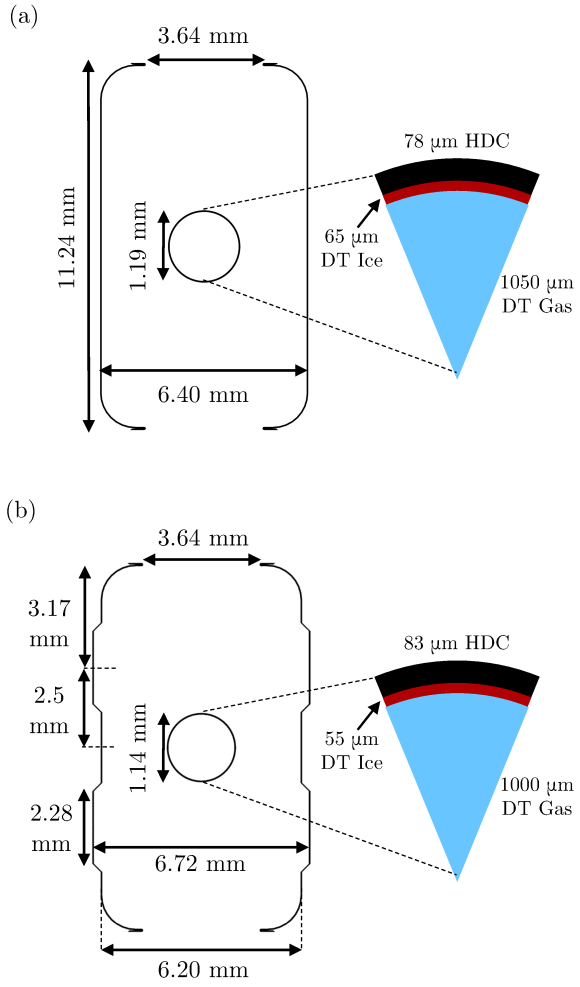

Fig. 4 | Target dimensions: Schematics of the HYBRID-E (a) and I-Raum designs (b) showing the nominal target dimensions for the hohlraums (left) and pie charts for the central DT-fuel filled capsules (right). The HDC ablator consists of a ~5μm inner un-doped HDC layer, followed by a Tungsten (W) doped HDC layer at larger radii, and an outer un-doped HDC layer. See Table 2 for additional design parameters.

convergence and velocities for a given ablator mass remaining given good capsule quality. Experiments at the 1050μm inner radius scale using thinner DT ice layers (10μm thinner) are currently being tested. Preliminary results show faster implosions velocities (+10-15km/s) at similar ablator mass remaining and levels of hot spot mixing. The tradeoff in ablator and DT ice thicknesses verses directly hydroscaling HDC[9,21] will be tested in future experiments using even more efficient hohlraums, see the Methods Future Studies section. These studies are imperative for understanding the design limitations of additionally increasing capsule scale within the experimental capability of NIF.

To maintain linear growth factors at both interfaces when hydroscalling, the prescription from Clark, *et al*[21] is to reduce the dopant concentration by the reciprocal of the scale increase. For the HYBRID-E N210207, the dopant was lowered to 0.28% W, consistent with this scaling as compared to the HDC design (W 0.33% and similar layer thickness). HYBRID-E experiment N201101 used an HDC capsule with higher optical depth, dopant concentration times dopant layer thickness, compared to the HDC design (see Table 2) but performed similarly to N210207 when accounting for the difference in the hot

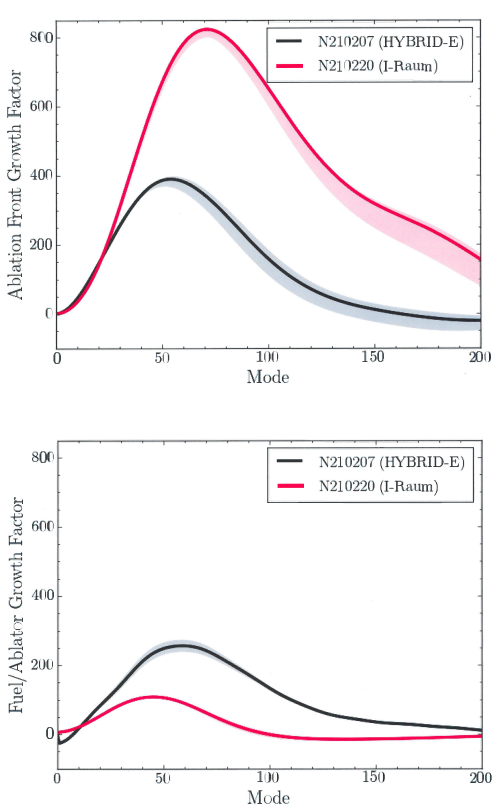

Fig. 5 | Linear growth factors for high-mode perturbations: Ablation front growth factors (AFGF) and fuel-ablator interface growth factors (FAGF) as a function of mode number at peak implosion velocity for HYBRID-E (black) and I-Raum (red), showing a tradeoff in design stability at the two interfaces due to differences in the dopant layer thickness. The shaded bands show the growth factors at ±50ps from peak implosion velocity.

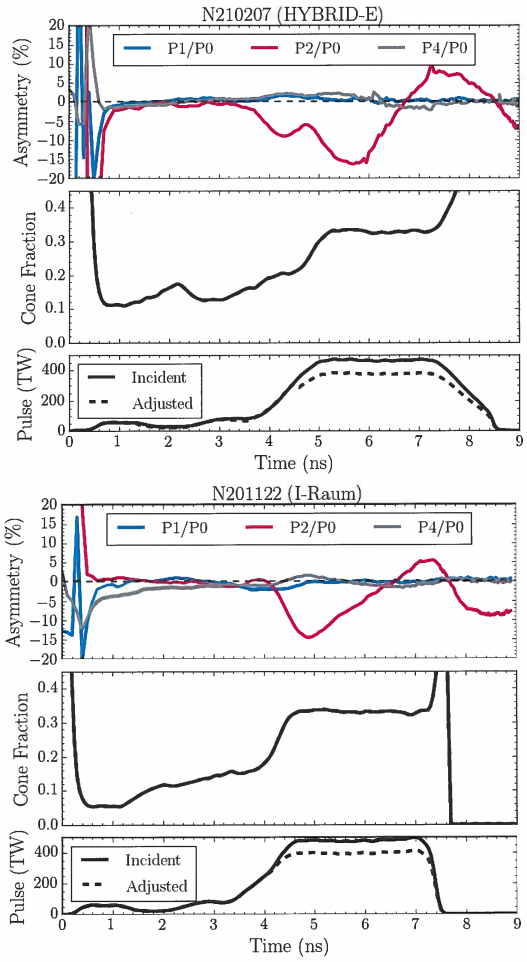

Fig. 6 | Radiation flux asymmetries: Calculated normalized Legendre decompositions of the radiation flux moments (P1/P0 in blue P2/P0 in red and P4/P0 in grey) as a function of time, with the incident cone fraction (ratio of inner power to total power) and laser power profiles shown below the radiation flux asymmetries for HYBRID-E (top) and I-Raum (bottom). The total laser power as a function of time is shown before and after drive multipliers are applied to the pulse to match experimental data.

spot and dense fuel symmetry. The doped layer of the I-Raum design was thicker than for HYBRID-E or than a scale of the HDC or Bigfoot designs which resulted in lower growth factors at the fuel-ablator interface and higher growth factors at the ablation front compared to HDC or HYBRID-E, see Fig.5. Uncertainties in the hohlraum atomic models used in this work could lead to growth factors at the ablation front that are ∼200 higher than shown in Fig.5 for both designs. Another factor when designing implosion stability is the early part of the laser pulse (called the "picket") which launches the first shock and blows down the ablation front. Higher early time ablation pressure can reduce perturbation growth factors at the ablation front. The HYBRID-E and I-Raum designs had similar first shock radiation temperatures, which was achieved with a lower picket power for HYBRID-E due to the smaller CCR where the outer beams hit the hohlraum wall compared to I-Raum. This led to similar first shock strengths (>12 Mbar), which were designed to avoid refreeze of the diamond behind the shock front and in the reflected shock, and similar fuel adiabats at peak velocity.

A short "coast" time, nominally the time between maximum radiation temperature and bang time (maximum compression), is important for maintaining ablation pressure and achieving high hot spot pressures and fuel compression,[22] but is more challenging with fixed laser energy and for maintaining symmetry. A ramped (or "drooping") laser pulse[3,10] was used in HYBRID-E which was designed to help maintain the late time ablation pressure at the larger scale while enabling the full use of the NIF laser (see Fig.6). For the experiments in this paper, the coast time as defined by 95% maximum T_r are similar but shorter for HYBRID-E due to the ramped laser power at the end of the pulse. A metric related to coast time is the deceleration time, R_{pv}/v_{imp}, where R_{pv} is the radius at peak velocity and v_{imp} is the implosion velocity, see Table 1. The increased deceleration rate associated with a short coast increases the rate at which implosion kinetic energy is turned into internal energy. For fixed v_{imp}, a larger scale implosion will have a longer deceleration time, so it is necessary to compensate for that by keeping the late-time hohlraum temperature hot (maintaining a higher late-time ablation pressure) via extending the duration of the laser pulse-shape, see Table 1 which was longer for HYBRID-E vs the I-Raum accounting for the scale factor. In the limit of zero coast time, the pressure inside the implosion, responsible for deceleration, rapidly overwhelms the ablation pressure outside the implosion and the impact of further extending the radiation drive is reduced. The designs in this paper have not yet seen a reduction in impact when reducing coast time and further improvements can be made in both platforms.

Deuterium-Tritium dense shell non-uniformities, or ρR variations, at peak compression, that can arise from early-time radiation flux asymmetries, are minimized by controlling the "foot" of the radiation drive,

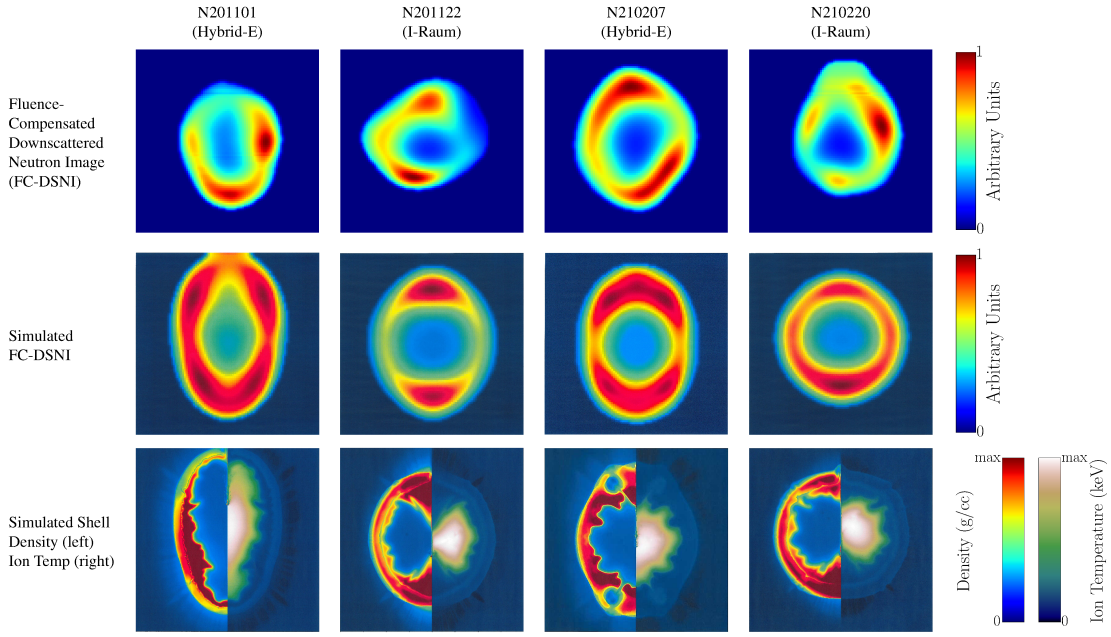

Fig. 7 | Shell and hotspot configurations at peak neutron production. Each image is 200 × 200 μm with color scale(s) normalized to the maximum value(s) in that panel. Top row: Measured fluence - compensated down-scattered neutron images (FC-DSNI) for each shot. Red indicates regions of higher areal density and neutron scatter. Center row: Simulated FC-DSNI images from 2D radiation-hydrodynamic capsule-only simulations for each shot with known degradations, including the capsule support tent and fill tube (low mode mix), surface roughness (high mode mix), x-ray drive asymmetries, and as-fabricated shell non-uniformity. Bottom row: Simulated density (left) and ion temperature (right) maps at peak neutron production. The maximum (density, ion temperature) values for each panel, left to right, in (g/cc, keV) are: (350, 7.31), (450, 6.49), (350, 8.4), (450, 7.2).

time until the rise to peak power, using cone fraction balancing. The cone fraction is defined as the ratio of inner laser power over the total laser power. The P2/P0 in the foot of the pulse (before the rise to peak laser power) is designed to be as close to zero as possible, but and allowed to swing during the peak of the pulse to enable full use of NIF (33% cone fraction), and may deviate from zero at early times due to as-shot laser delivery, see Fig.6. During the peak of the laser pulse, the inner beams can propagate easily initially and the radiation flux asymmetry has a negative sign in P2/P0 (or higher drive at the waist of the hohlraum). Near the end of peak power the inners have more difficulty propagating beyond the expanding wall and ablator material and the sign of the P2/P0 flux changes. Swinging flux asymmetry during the peak of the pulse is not detrimental to the implosion as long as the swing can be balanced to provide a symmetric final dense shell and hot spot where the symmetry of the implosion is not swinging. This is assessed in simulations and experiments through the shape of the implosion at $\sim$200μm compared to peak compression at $\sim$40μm. The P2/P0 flux asymmetry is similar in magnitude between the designs but changing sign faster for HYBRID-E due to the longer pulse and larger capsule, and also a result of requiring more transfer early in the pulse to compensate for the late time P2/P0 sign change. The primary impact of increasing CBET is to shift the P2/P0 radiation flux swing during the peak of the pulse to more negative values, while maintaining symmetry during the "foot", and does not significantly change the slope of the swing.[11]

Until the time when significant plasma filling and LEH closure come into play, radiation hydrodynamic simulations tuned to previous data are very predictive in designing symmetric shocks viewed along the pole and equator, a metric for "foot" P2 flux asymmetry, see the Methods section Simulation Methodology. As found previously, even when using cross-beam energy transfer to control symmetry during the peak of the pulse, radiation drive symmetry during the foot of the pulse can be accurately predicted and modeled with no artificial multipliers in low gas filled hohlraums.[4,11,12] The P4/P0 flux asymmetry is determined mainly by the CCR, picket power, and outer beam pointing. Changes between the designs lead to slightly worse calculated P4/P0 flux asymmetry for I-Raum compared to HYBRID-E in the "foot" of the laser pulse.

Simulation Methodology

Optimizations to the target designs were studied through numerical simulations (HYDRA[36]) and semi-empirical models were used to[27] guide design choices relating to the radiation drive symmetry during the peak of the laser pulse which is difficult to model.[11] The simulation methodology is performed in a two step process for designing the platforms and simulating the as-shot experiments which includes using the delivered laser pulse and measured target dimensions (hohlraum and capsule). The radiation hydrodynamic simulations include multi-group radiation transport, non-local thermodynamic equilibrium (NLTE) atomic kinetics, required for modeling high atomic number hohlraums and capsule ablation, using detailed configuration accounting (LLNL 2010 DCA atomic models),[5] three dimensional ray tracing for laser-light interaction with the hohlraum wall and plasma and detailed account of the transfer of energy between beams, detailed equation of state and opacity models, Monte Carlo transport of the fusion products, and electron thermal conduction from LEOS tables with a flux-limiter of $0.15 n_e T_e v_{Te}$. Here, n_e is the electron density, T_e is the electron temperature, and v_{Te} is the electron thermal velocity. First, lower spatial resolution integrated capsule and hohlraum simulations model the radiation drive with spatial, temporal, and photon energy resolution, see Fig.1. These simulations require calibration of the drive magnitude and symmetry during the peak of the pulse to match experimental measurements in separate focused or

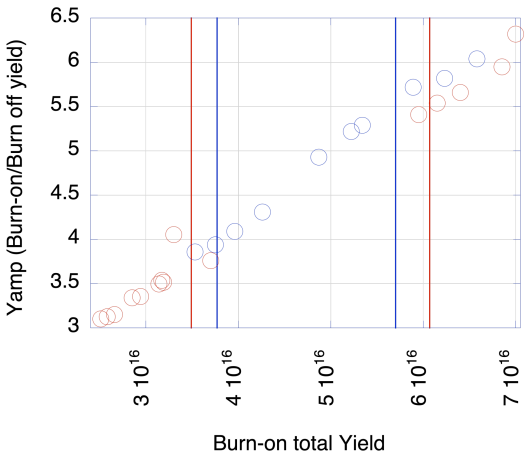

Fig. 8 | Neutron yield amplification from alpha heating: Calculated Yield amplification, ratio of total yield as a result of alpha particle heating to yield from simulations where the alpha particle heating is artificially turned off for HYBRID-E (red) and I-Raum (blue) as a function of total yield. Each point is a high resolution capsule simulation which applies different combinations of the known perturbations. The lines correspond to the total measured yields from the four experiments discussed int the main text (N201101, N201122, N210207, and N210220).

calibration experiments.[6,11,17]

The radiation drive is extracted from these lower resolution integrated hohlraum and capsule simulations and imposed on higher resolution capsule-only simulations[7,8] in two dimensions with symmetry along the axis, see Fig.7, which can resolve a larger number of modes ($\leq\sim$200). Also included are models[9] for the engineering features in the target (capsule support, fill tube, roughnesses of the capsule and ice layer) as well as the low mode perturbations from the radiation drive flux asymmetries. Fig. 7 shows a comparison of the simulated (middle) to measured fluence compensated down-scattered neutron image (FCDSNI)[10] (top), which provides a picture of the burn-averaged compressed dense shell surrounding the hot spot for the experiments in this paper. While the three dimensional features cannot be captured by two dimensional simulations, the main features and sizes of the compressed shells are generally reproduced, see also Table 1 for a comparison to other implosion metrics. For example, the higher density features at the poles for N201027 and N201122 are replicated by the simulations and low density region at the north pole for N201101 due to as-shot laser asymmetry is captured by the simulations. Simulated density and temperature images corresponding to these calculations at peak neutron production are shown in the bottom panel.

To calculate the amount of PdV work done on the hot spot we track a constant mass which encompasses 98% of the neutron production at peak neutron emission. The pressure and change in volume of this mass (with a volume weighting) are calculated to give the cumulative net PdV work on the hot spot, radiation loss from the hot spot, and alpha heating of the hot spot as a function of time, see Figure 3. This hot spot boundary is chosen to incorporate enough mass such that conduction losses are not significant. We use the PdV work calculated at the time of peak neutron production for the simulations where alpha particle heating is artificially turned off ("burn-off"), as alpha heating can increase the pressure and work done on the hot spot, but is similar to the the "burn-on" simulations. Ratios of the alpha heating energies to work done on the hot spot at "bang-time", and in total, are main metrics for a burning plasma.

The yield amplification (Y_{amp}), ratio of the neutron yield in simulations which allow the alpha particles to redeposit energy to simulations where this is artificially prohibited, is another metric for the impact of alpha particle heating on the implosion and a burning plasma. The performance of the HYBRID-E and I-Raum designs can be matched in two dimensions using a subset of the known degradations, and under-predict performance when all degradations are applied. To assess the impact of perturbation choice on the calculated yield amplification, various simulations of these designs including different perturbation choices or magnitude of the perturbations were performed, e.g. variations in surface roughness, tent model, fill tube model, low mode asymmetries, capsule thickness non-uniformities, and mix model at the fuel-ablator interface. Figure 7 shows a clear trend in Y_{amp} with total neutron yield for HYBRID-E (red) and I-Raum (blue) even for simulations with varying calculated down scattered ratios, a measure of the areal density of the compressed shell. The red and blue lines correspond to the total yields for the experiments in this paper, showing that all four experiments are calculated to meet the yield amplification criteria for a burning plasma of $>$3.5.

Future Studies

Future studies are aimed at continuing to optimize key metrics from equation 1. Fielding smaller laser entrance holes (LEH) from the present value of 3.64 mm to 3.1 mm, will improve the late-time ablation pressure by maintaining higher Tr later in time (less radiation losses). In addition, smaller LEH hohraums can achieve similar radiation temperatures to the designs in this work at lower power which enables longer duration pulses, even with fixed available laser energy, further improving the late time ablation pressure. The smaller LEH hohlraums can also be used to field thicker ablator implosions, e.g. $>4\mu$m thicker at the 1050μm inner radius scale and $>10\mu$m thicker at the 1100μm inner radius scale, which is expected to improve the design stability and enable higher implosion velocities with similar levels of ablator mass remaining. Based on the modest levels of CBET presently needed to control symmetry (Fig. 1b), we expect achieving adequate symmetry in a smaller LEH hohlraum to be manageable. The impact of DT ice layer thickness is also being investigated. Simulation studies that increased implosion convergence through reductions to implosion adiabat, while also controlling the tendency of more hydrodynamic instability are also being performed. Finally, experiments to further increase the implosion scale by 5-30% while maintaining the other critical properties in equation 1 are underway.

1. O. A. Williams, M. Nesládek, *physica status solidi (a)* **203**, 3375–3386 (2006).
2. L. Berzak Hopkins, L. Divol, C. Weber, S. Le Pape, N. B. Meezan, J. S. Ross, R. Tommasini, S. Khan, D. D. Ho, J. Biener, E. Dewald, C. Goyon, C. Kong, A. Nikroo, A. Pak, N. Rice, M. Stadermann, C. Wild, D. Callahan, and O. Hurricane, *Physics of Plasmas* **25**, 080706 (2018).
3. L Berzak Hopkins, S LePape, L Divol, A Pak, E Dewald, D D Ho, N Meezan, S Bhandarkar, L R Benedetti, T Bunn, J Biener, J Crippen, *et. al*, *Plasma Physics and Controlled Fusion* **61**, 014023 (2019).
4. L. A. Pickworth, T. Dppner, D. E. Hinkel, J. E. Ralph, B. Bachmann, L. P. Masse, L. Divol, L. R. Benedetti, P. M. Celliers, H. Chen, M. Hohenberger, S. F. Khan, O. L. Landen, N. Lemos, B. J. MacGowan, D. A. Mariscal, P. A. Michel, M. Millot, A. S. Moore, J. Park, M. B. Schneider, D. A. Callahan, and O. A. Hurricane, *Phys. of Plasmas* **27**, 102702 (2020).
5. MEHUL V. PATEL, HOWARD A. SCOTT, and MICHAEL M. MARINAK, *Abstract for the 52nd Annual Meeting of the APS Division of Plasma Physics* **55**, , http://meetings.aps.org/link/BAPS.2010.DPP.NO5.8(2010).
6. O. S. Jones, C. J. Cerjan, M. M. Marinak, J. L. Milovich, H. F. Robey, P. T. Springer, L. R. Benedetti, D. L. Bleuel, E. J. Bond, D. K. Bradley, D. A. Callahan, et al, *Physics of Plasmas* **19**, 056315(2012).
7. D. S. Clark, D. E. Hinkel, D. C. Eder, O. S. Jones, S. W. Haan, B. A. Hammel, M. M. Marinak, J. L. Milovich, H. F. Robey, L. J. Suter, and R. P. J. Town, *Phys. of Plasmas* **20**, 056318 (2013).

8. D S Clark, A L Kritcher, J L Milovich, J D Salmonson, C R Weber, S W Haan, B A Hammel, D E Hinkel, M M Marinak, M V Patel and S M Sepke, *Plasma Phys. Control. Fusion* **59**, 055006 (2017).
9. , , ().
10. D. T. Casey, P. L. Volegov, F. E. Merrill, D. H. Munro, G. P. Grim, O. L. Landen, B. K. Spears, D. N. Fittinghoff, J. E. Field, and V. A. Smalyuk, *Review of Scientific Instruments* **87**, 11E715(2016).